Near-infrared noise in intense electron bunches

Sergei Kladov,[1,*] Sergei Nagaitsev,[2] Young-Kee Kim,[1] Daniel R. Broemmelsiek,[3] Zhirong Huang,[4] Jonathan Jarvis,[3] Alex H. Lumpkin,[3] Jinhao Ruan,[3] Andrea Saewert,[3] and Randy M. Thurman-Keup[3]

[1]*University of Chicago, Chicago, Illinois, USA*
[2]*Brookhaven National Laboratory, Upton, New York, USA*
[3]*Fermi National Accelerator Laboratory, Batavia, Illinois, USA*
[4]*SLAC National Accelerator Laboratory, Menlo Park, California, USA*

(Received 10 February 2025; accepted 18 December 2025; published 23 January 2026)

This article investigates electron bunch density fluctuations in the $1-10$ μm wavelength range, focusing on their impact on coherent electron cooling (CEC) in hadron storage rings. In this study, we compare the shot-noise model with experimental observations using bandwidth-filtered near-infrared optical transition radiation (OTR) photodiode signals, where the transverse bunch size is much larger than the OTR wavelength of interest. The relativistic electron bunch ($\gamma \approx 50$) parameters are close to those proposed for the coherent electron cooler in the electron-ion collider (EIC) project. Preliminary feasibility experiments were conducted, and the noise factors are presented, supported by particle tracking. No major density fluctuations or effective cooling rate decrease were revealed for EIC CEC design parameters. Additionally, longitudinal-space-charge-induced microbunching for the chicane-compressed bunch was observed with coherent OTR enhancements up to 100 times, providing further calibration of the measurement method.

DOI: 10.1103/c3fd-g5mn

I. INTRODUCTION

The significance of bunch quality in relativistic electron bunches became increasingly prominent as the allowed density fluctuations, often called "noise," approached the Poisson statistics level (shot noise [1,2]). It is important in various applications, including high-energy hadron cooling systems [3,4] and free-electron lasers (FELs) [5,6].

The modulation is defined as the difference between the unperturbed distribution function, $\rho_0(t)$, and the actual distribution function, $\rho(t)$. The unperturbed distribution $\rho_0(t)$ neglects the rigidity of the electrons, whereas the actual distribution $\rho(t)$ consists of N electrons arriving at times t_j, represented by Dirac delta functions. It is more convenient to analyze the modulations in the Fourier domain (spectrum):

$$\delta\rho_e(\omega) = \rho(\omega) - \rho_0(\omega) = \frac{1}{N}\sum_{j=1}^{N} \mathrm{e}^{-i\omega t_j} - \rho_0(\omega), \qquad (1)$$

where j is the particle index and the distribution functions are normalized on 1. The actual Fourier spectrum is traditionally called *bunching factor* $\rho(\omega) = b(\omega)$ [7]. Propagation in basic elements that significantly change the spectrum, such as chicanes, has been well studied, including longitudinal space charge and coherent synchrotron radiation (CSR) (see Refs. [8–10] and references therein).

In this paper, we are focused on the electron bunch noise in a specific system, EIC CEC, described below, and on the measurement of the noise when the transverse bunch size is much larger than the observation wavelength.

The luminosity in colliders depends mainly on bunch intensities and emittances, which in turn depend on many factors and processes, such as intrabeam scattering [11]. To maintain hadron bunch quality and high brightness, bunch cooling can be implemented in storage rings. Currently, two methods are employed: electron cooling [12] and stochastic cooling [13,14]. While electron cooling has been extensively studied and widely implemented, its cooling rate drops significantly with energy increase [15], with the highest hadron energy cooled by this method being 8.9 GeV [16].

Stochastic cooling functions as a broadband feedback system by damping hadron bunch density fluctuations, detected by a "pick-up" device, amplified, and then applied to a "kicker" device at an optimal signal phase. Its cooling rate is not strongly dependent on bunch energy and is also proportional to the device's operational frequency [15], making optical stochastic cooling (OSC) [17], for example, orders of magnitude more effective than microwave

*Contact author: kladov@uchicago.edu

Published by the American Physical Society under the terms of the Creative Commons Attribution 4.0 International license. Further distribution of this work must maintain attribution to the author(s) and the published article's title, journal citation, and DOI.

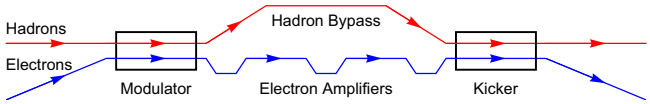


FIG. 1. Coherent electron cooling (CEC) scheme.

stochastic cooling schemes and even more so than electron cooling at high energies [18]. Like the OSC method, coherent electron cooling (CEC) is a variation of transit time stochastic cooling, where the same electron bunch acts as both the pick-up modulator and the kicker [19–21]. Initially, the electron bunch receives a longitudinal density imprint, shaped by the hadron bunch [22]; this kick is then amplified and transformed into longitudinal density modulation by a chicane, and finally, the hadron bunch is kicked by the modulated electron bunch with a specific phase shift, achieving cooling. The basic system scheme, to be built at the electron-ion collider (EIC), is depicted in Fig. 1 [23].

Additional electron bunch density modulations introduce extra diffusion in the hadron bunch, counteracting cooling [3,4,24]. The evolution of the longitudinal hadron bunch emittance, ε_L, is determined by [22]

$$\frac{1}{\varepsilon_L}\frac{d\varepsilon_L}{dt} = -\frac{1}{T_{\mathrm{cool}}} + \frac{D}{\varepsilon_L}, \tag{2}$$

where ε_L/D is the characteristic diffusion time, T_{diff}, and $1/T_{\mathrm{cool}}$ is the optimized cooling rate with no noise taken into account. The diffusion coefficient D contains contributions from both the hadron bunch and the electron bunch density fluctuations. The hadron bunch density fluctuations are Poisson-distributed (shot noise), and their contribution is well studied in [3,4]. Following the notations from [3], it can be described by the ratio of the rates:

$$\frac{T_{\mathrm{cool}}}{T_{\mathrm{diff}_h}} = r_1, \tag{3}$$

where T_{diff_h} is the characteristic time of the diffusion caused by the shot noise in the hadron bunch, and $r_1 = 0.04$ for EIC parameters [23].

Therefore, we focus our attention on the electron bunch noise only. The shot level noise taken into account at the entrance to the amplifier section is treated similarly and results in a similar expression:

$$\frac{T_{\mathrm{cool}}}{T_{\mathrm{diff}_e}} = r_2, \tag{4}$$

where $r_2 = 0.02$ for EIC parameters. Besides the base effect r_2, the electron noise contribution contains an effect in the modulator, as well as the interference term [4]. Following Appendix A, we neglect these terms and also take into account the density fluctuations that are different from the shot noise:

$$\frac{T_{\mathrm{cool}}}{T_{\mathrm{diff}_e}} = r_2 \frac{\int_{-\infty}^{\infty} |Z_{e,2}(\omega)|^2 |\delta\rho_e(\omega)|^2 \, \mathrm{d}\omega}{\int_{-\infty}^{\infty} |Z_{e,2}(\omega)|^2 \frac{1}{N} \, \mathrm{d}\omega}, \tag{5}$$

where $r_2 = 0.02$ is the ratio for a shot-noise (quiet) bunch, N is the number of electrons in the bunch, and $Z_{e,2}(\omega)$ is the total impedance of the CEC amplifier and kicker sections for pre-existing electron density modulations $\delta\rho_e(\omega)$.

The impedance (Fig. 2, left), which is the Fourier transform of the temporal "kick," applied to hadrons (Fig. 2, right), is a convenient tool, broadly used by the CEC community [3,4]. If wakes are used, Eq. (5) transforms to a heavier expression without an obvious connection to experimental measurements. Note that the system's response characteristic length is about 1 μm.

It can be seen from Eq. (5) that the effective cooling time decreases significantly even when the spectral power in the near-infrared (NIR) region is not much larger than the shot level $|\delta\rho_e(\omega)|^2 = 1/N$. Noise comparable to $1/N$ is called "low-level" throughout the paper, and its NIR part presents the main interest of the study.

The same noise is also relevant in FELs. In self-amplified spontaneous emission and self-seeded FELs the microwave instability starts from the initial noise in the bunch, leading

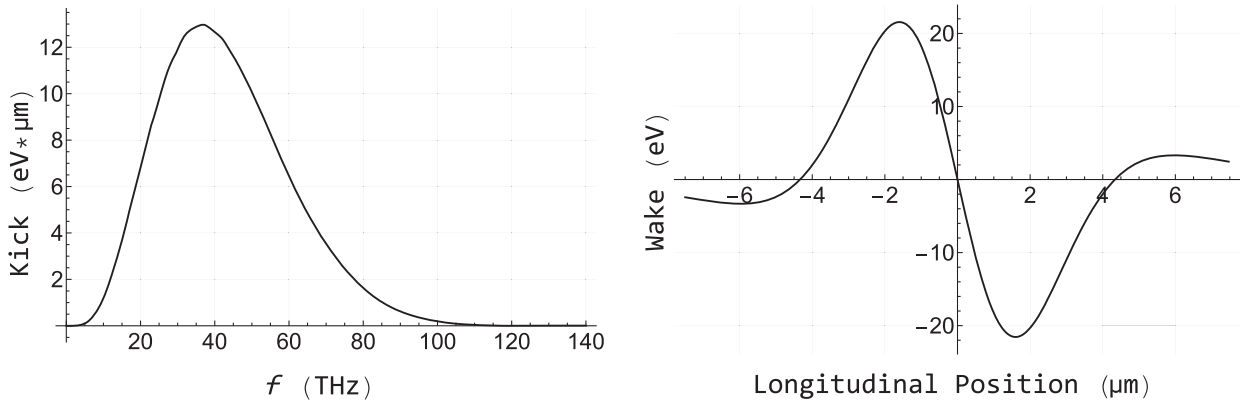


FIG. 2. Total impedance of the coherent electron cooling (CEC) amplifier and kicker sections at EIC in the frequency ($f = \frac{1}{2\pi}\omega$) domain and the wake function in the spatial ($z = ct$) domain. The characteristic length is 1 μm.

to the bunch microbunching and resulting in coherent radiation. Hence, the initial noise within the FEL bandwidth plays a beneficial role [5]. Conversely, in externally seeded FELs, such noise disrupts the seed signal, and reducing noise at the initial seed wavelength can lower the seed laser power requirements. The dynamics of noise in HGHG FELs was analyzed in Ref. [25], while its approximate effects on HGHG FELs were studied in Ref. [6]. A more detailed description of noise effect on the radiation from a single undulator is given in Ref. [26].

There have been several proposals in the past to suppress the noise, for example, with a broadband laser amplifier [27] or in a drift section [28] (and references therein). However, before suppressing the noise it is necessary to understand its amplitude and spectral decomposition, as well as its origin. Although the noise exceeding shot level has been already observed in linear electron accelerators without external wavelength modulation [29], there is no comprehensive analysis and simulation support for low-level fluctuations, especially in the range of bunch parameters similar to EIC CEC.

In this paper, we present measurements of the electron bunch density noise level in the 0.5–3 μm wavelength range, and compare them with analytical and tracking predictions. We show that if the bunch has parameters similar to ones in the proposed EIC CEC scheme, it does not have major fluctuations in the NIR region, while the noise becomes much stronger if the bunch is longitudinally compressed.

The article is organized as follows. In Secs. II and III, we give an overview of the experiment: general idea and technical details. It is followed by Sec. IV, devoted to providing a theoretical basis for predicting and analyzing the experimental data. This data are presented in Sec. V, alongside a discussion. Next, the simulations and the tracking results are briefly described in Sec. VI. Finally, Sec. VII contains a discussion about the compressed beam and the elevated noise, together with a list of addressed issues and effects.

The electron bunch noise influence on the cooling rate at EIC CEC is described in Appendix A. Appendix B provides a detailed study of the optical channel, necessary for experimental data understanding, and Appendix C summarizes the main numerical values used in the article.

II. METHODS

Density fluctuations in electron bunches are traditionally measured by means of transition radiation (TR). The connection between the density fluctuations in the bunch and the TR signal has been well established in FELs, where the space charge impedance in a long linear accelerator, as well as strong compression to a high peak current, often results in bunch microstructures [30]. This microbunching strongly amplifies the TR in the optical range of frequencies, known as coherent optical transition radiation (COTR) [31].

The OTR energy per unit frequency ω per unit solid angle, radiated by a bunch of charged particles, traversing an ideal conducting plane, can be approximated as (see Sec. IV A):

$$\frac{d^2W}{d\omega d\Omega} = \frac{d^2W_1}{d\omega d\Omega} N^2 |\rho(\omega)|^2, \tag{6}$$

where $\rho(\omega)$ is the Fourier spectrum of the normalized longitudinal bunch density distribution function ($\rho(0) = 1$), and $\frac{d^2W_1}{d\omega d\Omega}$ is the spectrum for one particle. Note that this approximation is valid only when the bunch size is small: $\sigma_\perp \ll \lambda\gamma$. The single-particle spectrum is given by

$$\frac{d^2W_1}{d\omega d\Omega} = \frac{Z_0 q^2}{4\pi^3} \frac{\beta^2 \sin^2\theta}{(1-\beta^2\cos^2\theta)^2} \approx \frac{Z_0 q^2}{4\pi^3} \frac{\theta^2}{(\gamma^{-2}+\theta^2)^2}, \tag{7}$$

where $\beta = v/c$ is the particle velocity normalized by speed of light, $Z_0 \approx 377\ \Omega$ is the impedance of free space, q is the single-particle charge, and the relativistic factor is $\gamma \gg 1$. The single-particle spectrum is written for the conducting plane (foil) perpendicular to the particle trajectory. The angle θ is the angle between the normal vector to the plane and the emission direction.

In this ultrarelativistic case, most of the OTR radiation is concentrated in a cone with $|\theta| < 1/\gamma$. Therefore, the photons can be efficiently transported from the foil to the detection system. It is also seen from the expression that an elevated level of noise results in a higher energy of the radiation, possibly with a spiky spectrum, and faster signal scaling with charge (e.g., quadratic). Assuming a bunch charge of 1 nC, the radiation energy W per quiet bunch (shot noise, $|\rho(\omega)|^2 = 1/N$) in the band $\Delta\lambda = 100$ nm, $\lambda_0 = 1$ μm at 25 MeV is $W = 2.4$ pJ.

III. EXPERIMENTAL SETUP

The experiments were performed at Fermilab Accelerator Science and Technology (FAST) facility as it can provide electron bunches with similar bunch parameters as in the EIC CEC concept. The comparison is presented in Table I. The most important parameters for this project are summarized in Appendix C.

The data were collected from the existing diagnostics cross X121 (see Fig. 3), where a YAG:Ce scintillator screen and an OTR screen are installed and viewed by a CCD and

TABLE I. FAST and proposed CEC bunch parameters.

Parameter	FAST	EIC
E_p, GeV		100–275
E_e, MeV	40–300	50–150
Bunch charge, nC	0–3	1
ε (rms, norm), μm	3 (at 1 nC)	2.8
rms bunch length, mm	0.3–10	12–8
Drift section, m	80	100

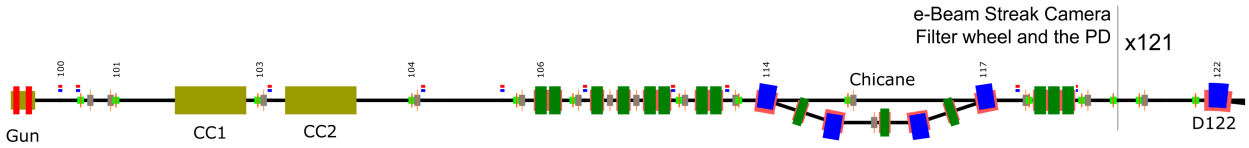


FIG. 3. FAST layout used in the experiment. A chicane follows two cryogenic rf cavities, compressing the bunch before diagnostics cross X121, where an Al-coated Si substrate acts as an optical transition radiation (OTR) screen. All the quadrupoles except the last triplet before the cross are turned off.

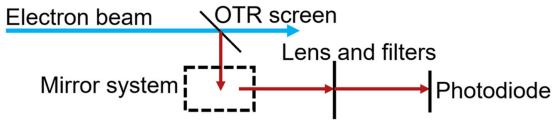


FIG. 4. Principal experimental scheme: TR spectrometer.

a streak camera, respectively. The bunch parameters were thus controlled in three dimensions by a chicane and quadrupoles.

The principal experimental apparatus, shown in Fig. 4, starts with an Al-coated Si substrate—a thin highly reflective foil (the OTR source), inserted into the bunch line at 45° with respect to the bunch direction. The emitted radiation energy is transported through an optical channel, passed through one of the available 12 NIR band-pass filters with bandwidth centers ranging from 750 to 2400 nm, and focused onto a sensitive photodiode.

The transport line consists of two parabolic mirrors with the foil and the photodiode located in the corresponding focal points and six highly reflective flat mirrors. The optical signal leaves the vacuum chamber through SiO_2 (fused silica) glass window with a cutoff transmittance wavelength of 3 μm. Detailed specifications of the optical channel and detector are summarized in the Appendix B.

The photodiode signal is transformed to voltage by means of a high-gain integrating amplifier, shown in Fig. 5 alongside the diode responsivity. This detector has low response at the red end of the visible-light regime, and maximum response in the 1800–2500 nm regime. The detector was calibrated in the same way as the previous amplifier [32] using two different laser systems.

The transmission functions of the filters used were measured at UChicago Soft Matter Characterization Facility using the Shimadzu—UV-3600 Plus (UV-VIS-NIR Spectrophotometer) with three detectors (PMT, InGaAs, PbS), allowing accurate transmission measurements in a wide wavelength range (185–3300 nm).

Two examples of the measurement results are presented in Fig. 6 [33]. The functions being far from the desired 100-nm-bandwidth ideals result in a significant complication to the data analysis (see Sec. IV).

IV. THEORETICAL EXPECTATIONS

A. OTR spectrum

Single particle. The OTR energy spectrum of one particle with charge q, passing through a metallic foil (screen), is well described in the literature. For example, Ref. [34] describes a particle passing through a plane orthogonal to its motion. We slightly modify the particle and mirror charge velocities to take into account the angle θ_p between the normal vector to the plane $\boldsymbol{n}_p = (\sin\theta_p, 0, \cos\theta_p)$ and the particle velocity $\boldsymbol{\beta}_1 = \beta_0\,(0, 0, 1)$. The mirror charge velocity is $\boldsymbol{\beta}_2 = \boldsymbol{\beta}_1 - 2\,(\boldsymbol{\beta}_1\boldsymbol{n}_p)\boldsymbol{n}_p$.

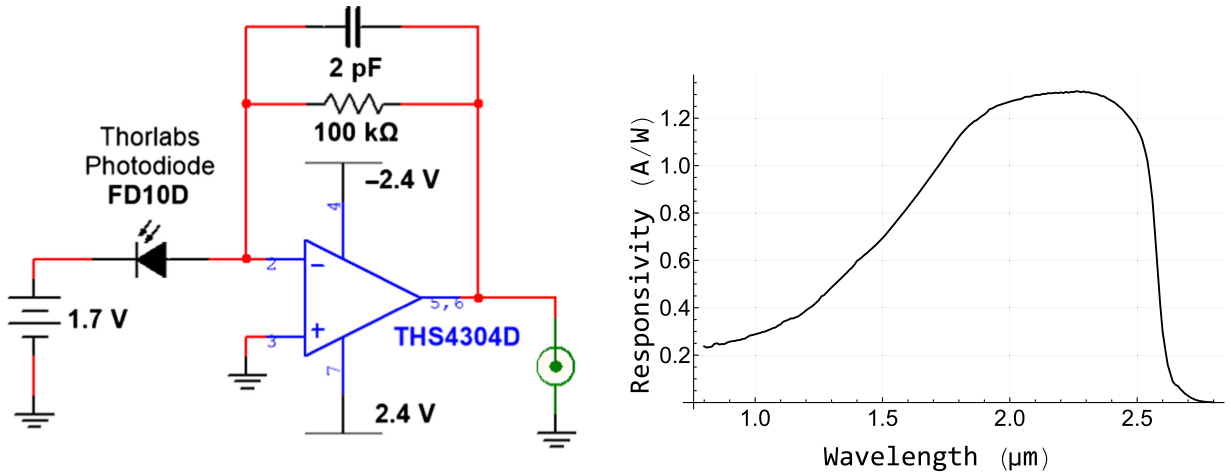


FIG. 5. Schematic of the amplifier circuit (left) and spectral response curve of the Thorlabs InGaAs photodiode FD10D (right).

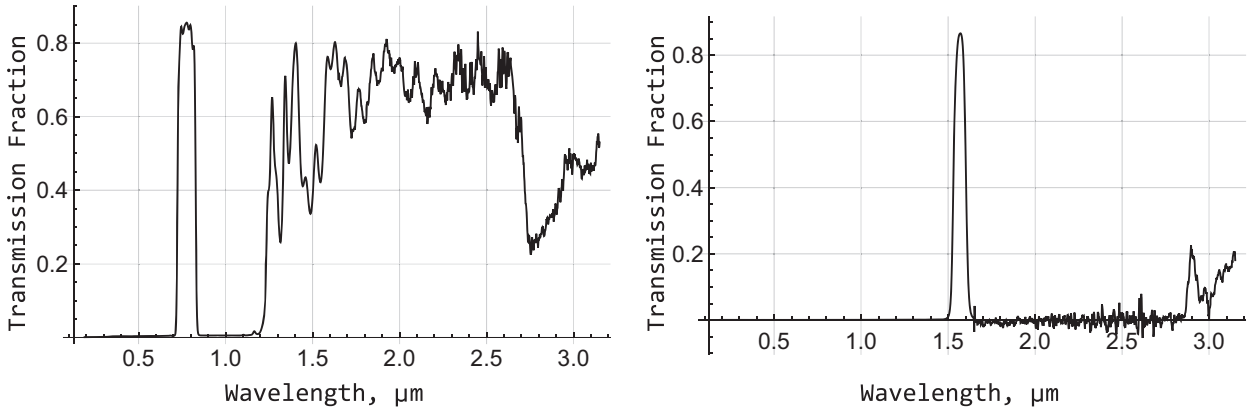


FIG. 6. Filter transmission functions at 770 nm (left) and 1570 nm (right).

Hence, the OTR energy spectrum from Eq. (25.49) of Ref. [34] becomes

$$\frac{dW_1}{d\omega d\Omega} = \frac{Z_0 q^2}{16\pi^3}\left[\frac{\boldsymbol{n}\times\boldsymbol{\beta}_1}{1+\boldsymbol{\beta}_1\boldsymbol{n}} - \frac{\boldsymbol{n}\times\boldsymbol{\beta}_2}{1+\boldsymbol{\beta}_2\boldsymbol{n}}\right]^2, \tag{8}$$

where $n = (\sin\theta\cos, \sin\theta\sin\phi, \cos\theta)$ is the direction of observation with angles (θ, ϕ). Note that, in contrast to Eq. (7), the particle velocity $\boldsymbol{\beta}_1$ is not necessarily parallel to the normal vector $\boldsymbol{n}_p$. The forward radiation is centered at $\theta = 0$, and the backward radiation is centered at $\theta = \pi - 2\,\theta_p$. Integration over the angles leads to the desired energy spectrum:

$$\frac{dW_1}{d\omega} = \int \frac{dW_1}{d\omega d\Omega}\sin\theta d\theta d\phi, \tag{9}$$

where the integration is taken by the half-space into which $-\boldsymbol{n}_p$ points. It is interesting to compute the integral for the specific case of $\theta_p = 0$:

$$\begin{aligned}\frac{dW_1}{\mathrm{d}\omega} &= 2\pi\int_0^{\pi/2}\frac{d^2W_1}{\mathrm{d}\omega d\Omega}\,\sin\theta\,\mathrm{d}\theta \\ &= \frac{Z_0 q^2}{4\pi^2}\left[\left(\frac{1}{\beta}+\beta\right)\mathrm{atanh}\,\beta - 1\right].\end{aligned} \tag{10}$$

In our case, the incident angle is close to $\pi/4$: $\theta_p = \pi/4 + p_x$, where p_x is the particle transverse momentum in radians. In practice, the integration boundaries are determined by the geometric restrictions, and the integral is computed numerically.

It will be helpful in the data analysis to express the energy spectrum in terms of the radiation wavelength:

$$\frac{dW_1}{d\lambda} = \frac{dW_1}{d\omega}\,\frac{2\pi c}{\lambda^2}. \tag{11}$$

N particles. Omitting the common multiplier, and assuming the transverse bunch size at the foil is negligible, the radiated energy spectrum can be written using the Fourier integral components [35] of electric fields:

$$\begin{aligned}\frac{dW}{d\omega} &\propto E_\omega E_\omega^* \propto \sum_{n=1}^{N} e^{i\omega t_n}\sum_{m=1}^{N} e^{-i\omega t_m} \\ &= N + \sum_{\substack{m,n \\ m\neq n}}\exp[i\omega(t_n - t_m)],\end{aligned} \tag{12}$$

where t_n is the arrival time of the nth particle $(n = 1, \ldots, N)$. Here we have assumed that the bunch is ultrarelativistic, and all the radiation is directed forward. The first and second terms are called "incoherent" and "coherent" transition radiation, respectively. If a bunch has transverse size larger than the observed wavelength, an additional factor $p(w)$ appears before the second term. Note that the expression can be rewritten as

$$\frac{dW}{d\omega} = \frac{dW_1}{d\omega}N^2|\rho(\omega)|^2. \tag{13}$$

For instance, $N = 1$ results in the single-particle spectrum, and a quiet bunch with N particles gives

$$|\rho(\omega)|^2 = \frac{1}{N} \quad \text{and} \quad \frac{dW}{d\omega} = N\frac{dW_1}{d\omega}. \tag{14}$$

It is convenient to relate the OTR spectrum to the spectrum of a quiet bunch using *noise factor F*, which is proportional to the bunching factor squared [7]:

$$F(\omega) = \frac{1}{N}\sum_{n,m=1}^{N} \mathrm{e}^{i\omega(t_n - t_m)} = N\,|b(\omega)|^2.$$

In the region of large frequencies $\omega \gg 2\,\pi\,c/\sigma_z$, the noise factor is proportional to the normalized modulation power introduced earlier:

$$F(\omega \gg 2\,\pi\,c/\sigma_z) \approx N\,|\delta\rho(\omega)|^2.$$

Therefore, it can be used in Eq. (5) directly. The noise factor equal to 1 for Poissonian (quiet) distribution of electrons.

With these modifications, Eq. (5) can be expressed in a simplified form:

$$\frac{T_{\mathrm{cool}}}{T_{\mathrm{diff}_e}} = r_2 \frac{\int_{-\infty}^{\infty} |Z_{e,2}(\omega)|^2 F(\omega) \mathrm{d}\omega}{\int_{-\infty}^{\infty} |Z_{e,2}(\omega)|^2 \, \mathrm{d}\omega}. \tag{15}$$

B. Total power

It is convenient to use wavelength notations λ instead of frequency ω when propagating the OTR spectrum through the measurement system. The voltage $U = (Q/C) = (1/C)\int I_c(t)dt$ on the capacitor due to the accumulated charge is

$$U = \frac{1}{C}\int I_c(t)dt = \frac{1}{C}\int r(\lambda)P(t,\lambda)dtd\lambda$$
$$= \frac{1}{C}\int r(\lambda)\frac{dW}{d\lambda}\Big|_{\mathrm{PD}} d\lambda, \tag{16}$$

where C is the capacitance, I_c is the current generated by the photodiode, $r(\lambda)$ is the PD responsivity in $[\frac{\mathrm{A}}{\mathrm{W}}]$, presented in Fig. 5, and $\frac{dW}{d\lambda}|_{\mathrm{PD}}$ is the spectrum of the radiation energy passed through a filter (at the photodiode). Here we assumed that all the charge, produced by the PD, settles on the capacitor because the bunch length is much shorter than the amplifier circuit RC time.

Because of the high leakage and broadbands of the filters, the map $\frac{dW}{d\omega} \to \frac{dW}{d\lambda}|_{\mathrm{PD}}$, connecting the TR spectrum before the transport channel and after passing through a filter is not even approximately reversible. Therefore, we choose the direct map at all three steps of the transformation from the bunch distribution to the set of observed signals (voltages) $\rho(\lambda) \to \{U_i\}$ and fit the data by repeatedly taking guesses of the distribution:

$$U_i = \int T_i(\lambda)\frac{N|\rho(\lambda)|^2}{\lambda^2}d\lambda = \int T_i(\lambda)F(\lambda)\frac{1}{\lambda^2}d\lambda, \tag{17}$$

where the noise factor is $F(\lambda) = N|\rho(\lambda)|^2$ and $T(\lambda)$ is the transmission function of the optical channel, including the photodiode responsivity and the capacitance C.

C. Optical channel

In order to account for the influence of the light transport channel, shown in Fig. 7, on the measured photodiode signal, we analyze the optical system formed by two parabolic mirrors. A rigorous treatment of the transport requires a simulation using the direct integration method. However, all the necessary estimations can be obtained using geometrical optics considerations. They reveal that each point on the OTR screen is imaged onto a unique point on the photodiode screen, independent of the emission angle. Furthermore, the optical path length does not depend on the emission angle either, implying that the phase of the radiation at the photodiode locally preserves the longitudinal coherence present at the OTR screen.

A spot with size d_p is formed on the photodiode screen even if a pointlike source on the OTR screen is considered (see Appendix B). This diffraction limit corresponds to the transverse extent over which the phase difference due to the spread of emission angles remains below λ, and is equal to $d_p = \gamma\lambda$. Therefore, the transport channel preserves the longitudinal coherence at the OTR screen only within the area of $s = \pi\gamma^2\lambda^2$. Different areas then add up incoherently to the photodiode total signal.

Additionally, geometric constraints such as the mirror apertures and the finite photodiode size further restrict the total detected radiation. For instance, we introduce the effective transverse bunch size $\sigma_{\mathrm{eff}} \approx \sigma_{\mathrm{PD}}$ (see Appendix C). Particles located farther than this effective radius from the optical axis on the OTR source are imaged, by the optical system, to positions outside the active area of the photodiode and thus do not contribute to the detected signal. We can write these results in analogy with Eq. (13), with expanded $|\rho(\lambda)|^2 = (1/N) + \frac{1}{N^2}\sum_{m,n;m\neq n}\exp[-2\pi i\,\frac{(z_n - z_m)}{\lambda}]$:

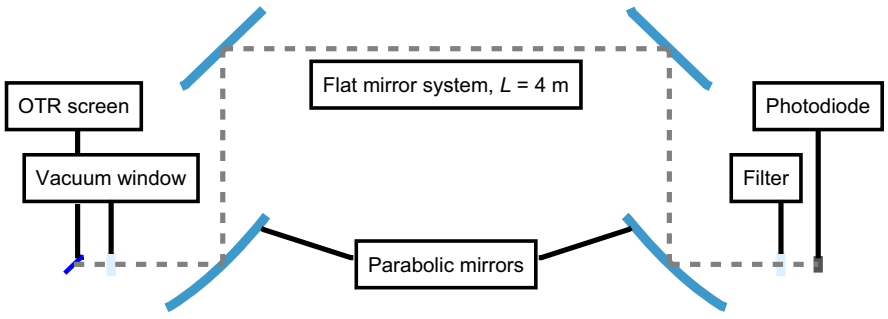


FIG. 7. Simplified schematic of the optical channel. The bunch generates transition radiation at the OTR screen (blue), then it is passed through a double-parabolic-mirror optical system (light blue, reflective), and is finally registered by the photodiode (gray). There are two transmission elements along the way: the vacuum window and a filter (dim blue). The OTR screen and the photodiode are located in the corresponding parabolic mirror focal points.

$$\left.\frac{dW}{d\lambda}\right|_{\mathrm{PD}} = \frac{dW_1}{d\lambda} N^2\, a(\lambda)\left(\frac{1}{N} + \frac{\gamma^2\lambda^2}{\sigma_{\mathrm{eff}}^2 N^2}\sum_{m,n}\exp\left[-2\pi i\,\frac{(z_n - z_m)}{\lambda}\right]\right), \tag{18}$$

where $\frac{dW}{d\lambda}|_{\mathrm{PD}}$ is the radiation power spectrum at the photodiode, $a(\lambda)$ is the total of the transmittance of the vacuum window and filter, the reflectance of the mirrors, and the fraction of the bunch charge within the effective transverse bunch size σ_{eff}. We call the value $p = \frac{\gamma^2\lambda^2}{\sigma_{\mathrm{eff}}^2}$ a "transverse coherence factor."

A detailed derivation of the transverse coherence factor, spot size, and geometric constraints, including explicit formulae and approximations, is provided in Appendix A. If summarized, the effective size is $\sigma_{\mathrm{eff}} \simeq 0.035$ cm, the emission angle limit is $|\theta|_{\max} \simeq 0.07$, and the mean contribution to $a(\lambda)$ from the bunch size $\sigma_\perp = 0.6$ mm is $a(\lambda)|_\sigma \simeq 0.15$. The transverse coherence factor with these parameters, at experiment energy of $\gamma = 50$, and at the wavelength $\lambda = 2$ μm is $p \simeq 0.08$. Of course, it depends quadratically on wavelength, so this value serves only as an order of magnitude. Nevertheless, we use $p \simeq 0.08 \pm 0.04$ when making theoretical predictions.

It should be noted that the bunch transverse size effect on OTR in a simple system without parabolic mirrors is widely studied [36,37]. Additionally, expressions for fields in empty space, generated by a general line source are derived by Nause *et al.* [38], where a comprehensive summary of how the effect was studied by different authors can also be found. Finally, these expressions were applied for a system with one focusing lens [39]. However, direct results from these papers are not directly applicable here due to a different measurement system. Also, simple estimates are enough for our purposes, meaning that the simulations based on the exact fields are not necessary.

V. EXPERIMENTAL RESULTS

The amplifier response to the TR signal is a typical curve of an RC circuit, where the RC time constant $\tau = 230$ ns is much larger than the bunch rms length $l = 10$ ps and the photodiode rise time $t_p = 25$ ns. In most measurements, the signal is averaged over 20 single shots. The signal saturation is treated by applying a fit to the rising part, whose slope is proportional to the signal amplitude. An example of an overshot signal is presented in Fig. 8 [33]. Of course, neutral density filters could be used to eliminate the saturation.

A. Low-level NIR noise

Comparison of the theoretical predictions for a shot-noise beam and experimental results is presented in Fig. 9. Here the combined reflectivity of the optical channel is taken to be $80 \pm 10\%$, and the transverse bunch shape—round Gaussian. X axis values are the means of the band-pass filters specified by the manufacturer; red is a set of the predicted voltage values, induced by the radiation passed through a set of filters; blue values are the measured voltages.

The uncertainties are present in both sides of the comparison, arising directly from the measurements on one side, and from the propagation of the guessed spectrum (flat here) through the measurement system [see Eq. (18)] on the other. While making the fit, we combine these uncertainties. In terms of the effect on the comparison, they can be split into two components: (i) Individual uncertainties at each filter: uncertainties in the scope data, uncertainties of the filter transmission function measurements, and bunch charge fluctuations; and (ii) Common multiplier at each filter: systematic uncertainties;

Individual uncertainties are depicted at both experimental and theoretical curves as error bars, while the systematic uncertainties are shown as bands.

The common multiplier uncertainty is composed of the uncertainties in the detector and beam distribution measurement accuracy: flat mirrors and vacuum window transmission functions (estimated as 10%), elements misalignment (see Appendix B), bunch size measurement uncertainty (estimated as 20% based on existing measurements), and, finally, the uncertainty of the calculations because of the bunch shape not being round (the maximum aspect ratio is taken as 1.2 based on the bunch profile

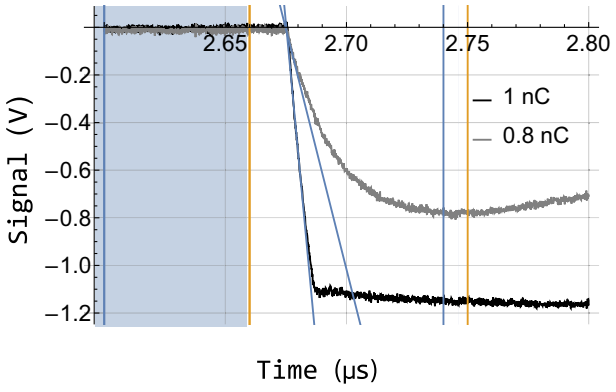


FIG. 8. Amplifier response to a single-bunch transition radiation pulse for two different bunch charges. The bunch here is compressed, the signal is amplified due to the coherent optical transition radiation (COTR). If the signal saturates, its amplitude is evaluated by its rising edge, approximated as a line. If not, the amplitude is found by subtraction of the dark current, averaged by the dashed area, from the signal extremum, averaged by the area between the second pair of vertical lines. For example, the signal for 1 nC is evaluated here as 2.24 ± 0.08 V, and for 0.8 nC as 0.7 ± 0.01 V.

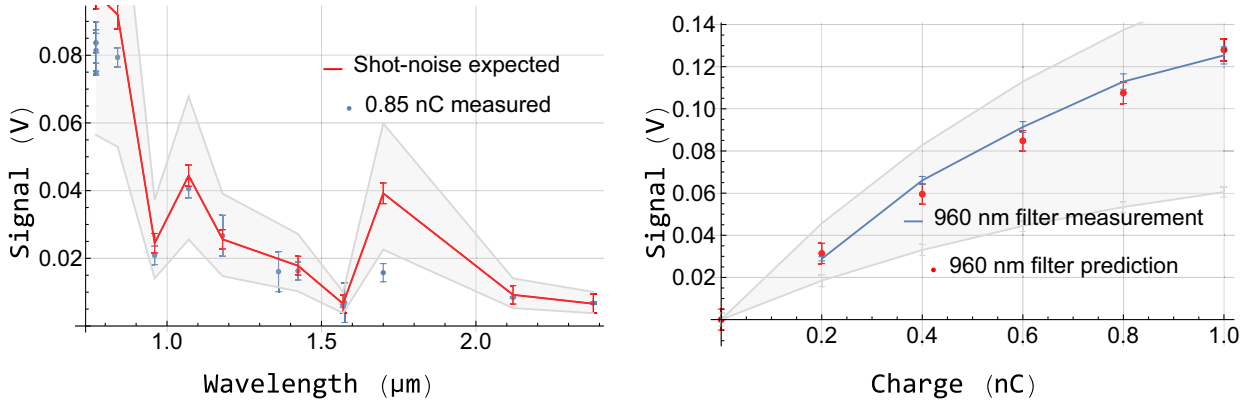


FIG. 9. Experimentally measured voltage induced by the optical transition radiation (OTR) and its comparison with the predictions based on the shot-noise bunch model. Left: comparison at different filters; right: comparison for different charges. The shaded area is a systematic uncertainty estimation.

measurements). In total, after the necessary propagation through the measurement system, it becomes $\Delta F = 30\%$.

The random uncertainty, composed of the bunch size and charge fluctuations (estimated as 10%), uncertainties of the filter transmission functions measurements (obtained during the measurements at UChicago), and signal fluctuations on the scope, are much smaller: $\Delta F = 5\%$ (average total of propagated uncertainty of the theoretical expectations and experimental measurements).

After performing a fit procedure with a constant function $F(\omega) = F$, and with uncertainties taken into account, the noise factor for the EIC CEC bunch parameters at 25 MeV can be estimated as $F = 1 \pm (0.3/p)$, where $p = 0.08 \pm 0.04$ is the transverse coherence factor. Of course, the noise factor cannot be negative, so instead of writing answers in $\pm$ form, we use a one-sided confidence interval. Therefore, with 67% confidence

$$F < 5,$$
$$\frac{T_{\text{cool}}}{T_{\text{diff}_e}} < 0.1. \tag{19}$$

B. Elevated NIR noise

The OTR signal increase has been previously observed in experiments with external modulation presence [40,41], which gives a peaked gain ($\frac{\text{COTR}}{\text{OTR}}$), and in experiments without any external excitation [31,42], giving a gain that is monotonically increasing with wavelength, starting at around 200 μm. Usually, the elevation becomes visible with bunch compression, when the characteristic length of the wavelength spectrum moves into the detector sensitivity range.

The FAST lattice used in this research is different from the facilities mentioned above in energy: $\gamma = 30 - 50$ instead of $\gamma = 200 - 400$. In this regime, the bunch is not rigid, and the particles are not tightly bound longitudinally. Therefore, we expect the elevation to appear at even smaller wavelengths.

Bunch rms length dependence on the second rf cavity (CC2) phase ϕ is presented in Fig. 10 left, alongside the simulated curve (see Sec. VI). The maximum compression factor achieved is $c = 8$ (from 8.5 to 1 ps), with the energy of the bunch kept constant.

Uncompressed and compressed bunch signals comparison is presented in Fig. 10 right. Here the bunch parameters are adjusted so that the signal increase is small for visibility. Although the increase in the signal is observed at all filters, it should be noted that the gain in emitted OTR cannot be obtained directly from the data because the filters have high leakage.

Taking broadband spectra as fit guesses gives unexpectedly poor results, predicting much higher gain at low-wavelength filters than it is observed experimentally, especially at 770 nm. It is due to the high broadband leakage these filters possess at higher wavelengths. On the contrary, filters with 1570, 2120, and 2380 nm labels are "pure," meaning that their transmission curves are almost like specified by the manufacturer.

Based on these features, it can be concluded that bunch spectrum has a spike at around 1.5 μm, and a broad elevation at wavelengths $\lambda > 2$ μm. Two examples of possible fits are presented in Fig. 11. No transverse coherence factor p is taken into account here.

Signal dependence on the bunch charge for various acceleration cavity phases is presented in Fig. 12. The shot-level signal (uncompressed bunch, left side) shows a linear dependence, while compressing the bunch (right side) leads to a highly nonlinear behavior.

The OTR power dependence on the second rf cavity (CC2) phase ϕ and rms bunch length σ_z is shown in Fig. 13. It is interesting that the difference in the extrema positions of the OTR power and bunch length dependence on ϕ can be used as a way to determine the initial amplitude of the energy modulations. In the first approximation it can be

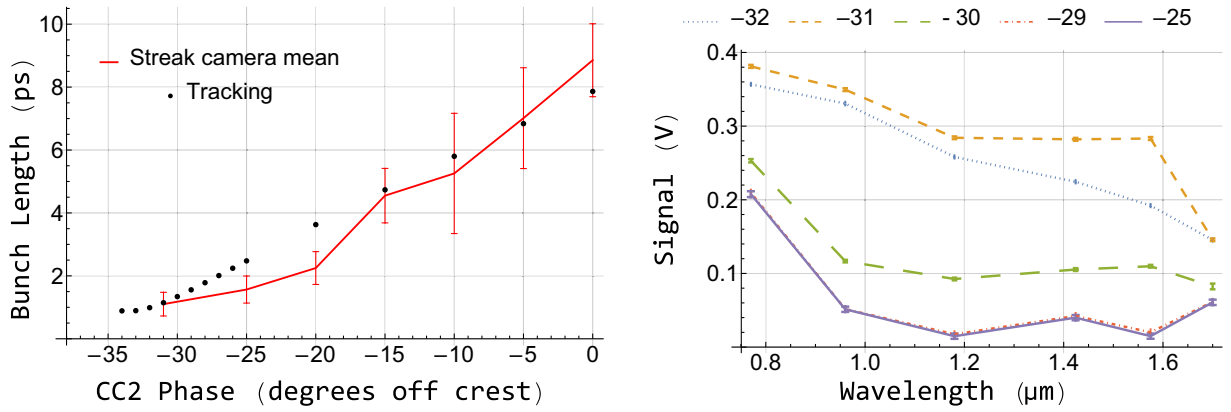


FIG. 10. Left: bunch rms length dependence on the second rf cavity (CC2) phase ϕ, obtained from the streak camera measurements and tracking simulations; the on-crest value is $\phi = 0°$. Right: the elevated signal for various ϕ, listed above the figure, and for filters, arranged along the X axis.

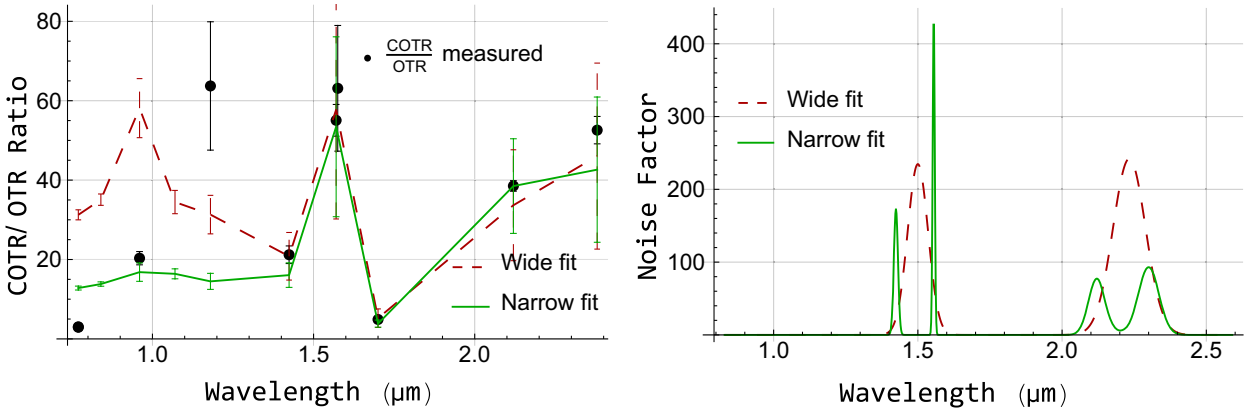


FIG. 11. Left: signal predictions based on a guessed spectrum and their comparison with the experimental data. Right: the guessed spectrum presented in terms of the noise factor (transverse coherence factor p is not taken into account here).

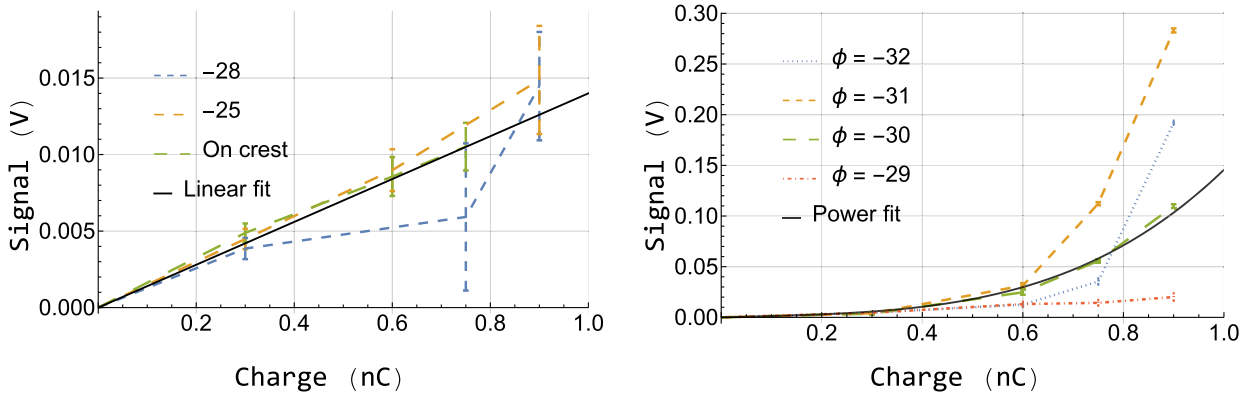


FIG. 12. Charge dependence of the observed signal for uncompressed (left) and compressed (right) bunch for different second rf cavity (CC2) phases ϕ, listed on the plots in degrees. Black line on the right is a power law fit with the power of $\frac{7}{2}$. The power is different from the expected Q^2 mostly because the bunch length, and hence the positions and intensity of the OTR spectrum peaks, depends on the bunch charge.

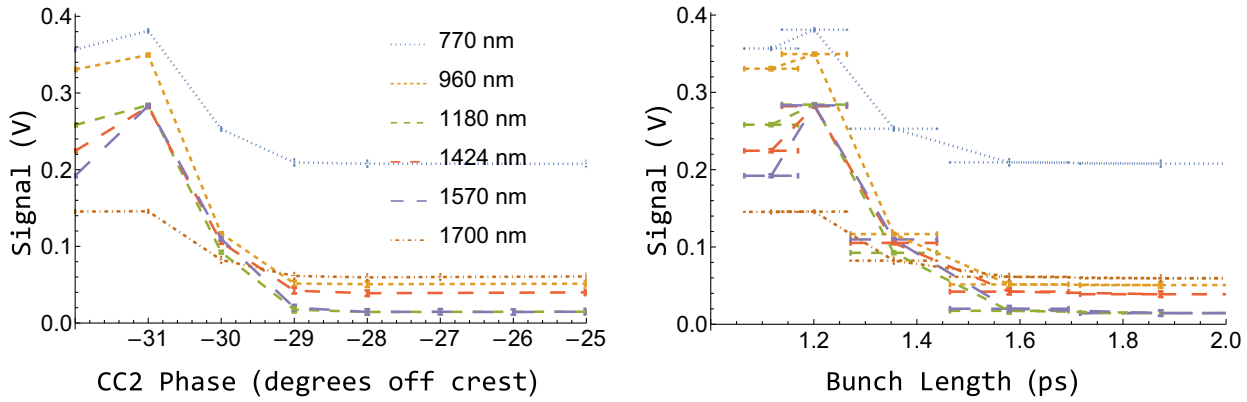


FIG. 13. Dependence of the OTR power on the second rf cavity (CC2) phase ϕ (left) and on the bunch rms length σ_z (right). The bunch length is calculated from the simulation results.

written as

$$\Delta E \approx E_{\mathrm{cav}} \frac{\omega_c}{\omega} (\sin\phi_1 - \sin\phi_2), \tag{20}$$

where E_{cav} is the energy that a particle gains from the second rf cavity (CC2) when it is on crest, ω_c is the cavity frequency, $\omega = \frac{2\pi c}{\lambda}$ is the bunch distribution modulation frequency, ϕ_1 is the CC2 phase where the bunch length is minimal, and ϕ_2 is the CC2 phase where the OTR radiation spectral component at wavelength λ is maximal. Of course, the high leakage of the filters used here makes this method too inaccurate, but getting a rough estimation is still possible.

C. OTR power fluctuations

The data were fitted assuming that the incoherent power did not change after the bunch compression. This assumption can be easily verified experimentally by looking at the intensity fluctuations. Indeed, if the histograms of the compressed and uncompressed bunch OTR signals intersect, according to Eq. (12), it means that the incoherent level was reduced. However, we do not see any intersection in the experiment.

The OTR intensity histograms for 1424 and 1700 μm filters at 1 nC for uncompressed (no microbunching) and compressed (with microbunching) bunches are presented in Fig. 14. The large fluctuations of the signal for compressed bunch are consistent with a coherent process starting from noise; the longitudinal-space-charge-induced microbunching in this case.

VI. SIMULATIONS

The space charge tracking was performed using ASTRA [43] at the cathode and accelerating part of the FAST lattice, followed by an s-based code ImpactX [44] responsible for the chicane. The space charge is taken into account using 3D Poisson solvers: FFT algorithm in ASTRA and "multigrid" in ImpactX. All the simulations are run on a personal computer, with ImpactX being parallelized on a GPU.

The simulations agree with the experiment in terms of general bunch properties, as illustrated in Fig. 10. We can transform the spectra into the expected signal using the same procedure as for the guessed spectra in Sec. V B. The

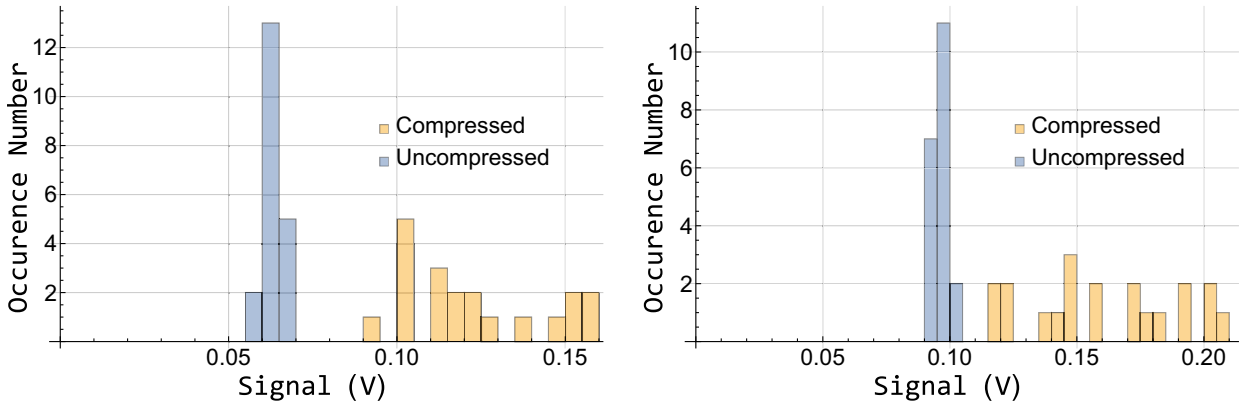


FIG. 14. Signal amplitude fluctuations for 1424 (left) and 1700 nm (right) filters at 1 nC. The distribution width is much larger if the signal is enhanced (compressed bunch), suggesting a coherent process starting from noise.

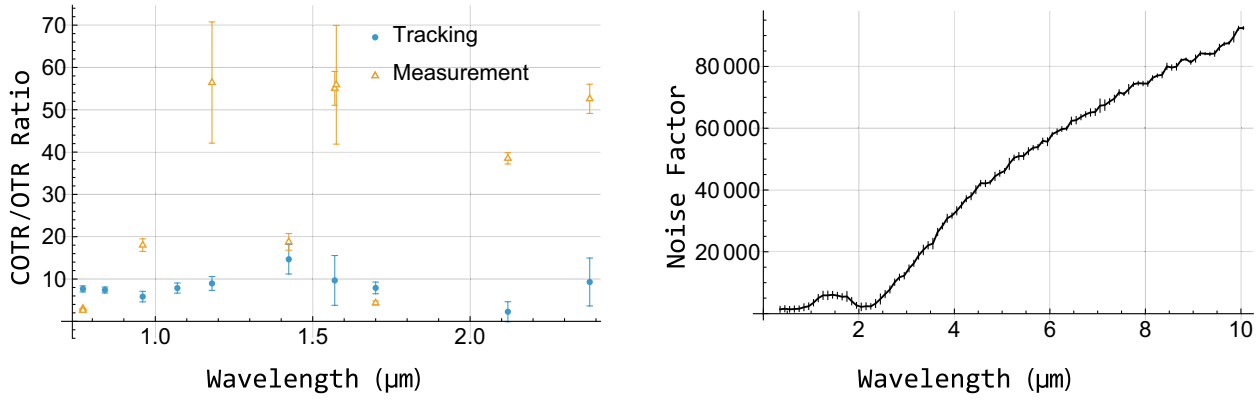


FIG. 15. Left: comparison of the raw experimental data, presented as the ratio of the signals from compressed and uncompressed beams (after the filters), and the same values but calculated from simulation results, with an assumption of the transverse coherence factor being $p = 0.08 \pm 0.04$. Right: the corresponding spectrum of the longitudinal bunch distribution, presented in terms of the noise factor.

data points obtained for each filter are presented in Fig. 15 left, alongside the experimental values for the second rf cavity (CC2) phase $\phi = -31°$ and the bunch charge is $Q = 1$ nC. The final simulated bunch longitudinal distribution spectrum in units of the noise factor is presented in Fig. 15 right. Because the simulations have only a limited number of particles, we scale the noise factor accordingly: $F_{\text{scaled}} = 1 + \frac{\sqrt{N}}{\sqrt{N_{\text{sim}}}}(F_{\text{sim}} - 1)$. It works well when the noise is elevated, but when the noise is sub-Poisson ($F < 1$), the scaled noise factor can become less than zero. We still use the scaling because we are interested in the elevated noise only.

The simulations present a valuable distinction from the experiment: the spectrum is known everywhere. Therefore, by establishing a connection between two approaches in the intersecting region ($0.7 - 2$ μm), we can estimate the experimental results at any wavelength for any compression factor. For instance, the noise factors obtained through tracking are presented in Fig. 16 for the second rf cavity (CC2) phases $\phi = -20$ (left) and $\phi = 0$ (right). A constant fit of the noise factor for the uncompressed bunch ($\phi = 0$) is $F = 0 \pm 10$ all the way up to $\lambda = 50$ μm—a range that covers the entire area of the EIC CEC impedance significance (see Fig. 2). The result was obtained from a list of fits with various bunch distribution binning and spectrum averaging. Again, the noise factor F cannot be less than 0, so we introduce an upper bound: with 67% confidence the noise factor is less than 10:

$$F < 10, \qquad \frac{T_{\text{cool}}}{T_{\text{diff}_e}} < 0.2. \tag{21}$$

VII. COMPARISON OF THE RESULTS

The uncompressed or moderately compressed bunch ($l > 2$ ps) has no additional noise above the shot level $F = 1$, which is supported by both the experiment and the space-charge particle tracking. This baseline is conserved after the bunch compression, with the coherent part revealing itself and reaching maximum at the second rf cavity (CC2) phase $\phi = -31°$. By comparing the simulated and experimental spectra for compressed bunches, we support the theoretical estimation of $p \approx 0.08 \pm 0.04$.

However, the individual filters' data are not in agreement. The difference is most likely caused by the

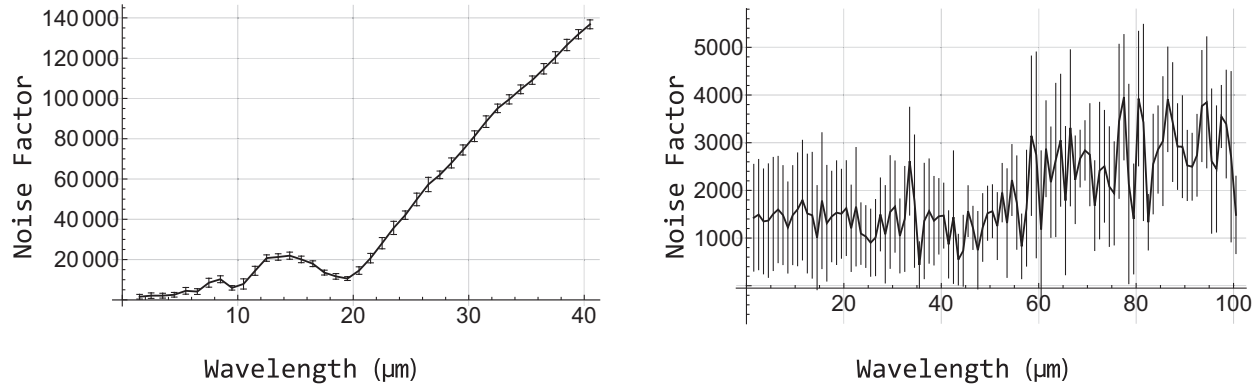


FIG. 16. Same as Fig. 15 right. Noise factor obtained from tracking for the second rf cavity (CC2) phase $\phi = -20$ (left) and $\phi = 0$ (right).

systematic uncertainties of the experiment: the transmission functions of the elements are not known exactly, and the bunch parameters were not controlled with enough precision due to a lack of theoretical predictions and tracking at the time of the experiment.

Nevertheless, other possible issues were also considered. The bunch energy is too high for wakefields to have such a major impact. Moreover, the characteristic short-range wakefield wavelength is 5 mm $\gg 1$ μm, and the lattice length is too short. Moving further, the bunch current is not high enough for CSR to noticeably change the bunch dynamics in the NIR region.

The signal increase might be explained by another type of radiation, reflected from the OTR screen. Examples include CSR or coherent optical edge radiation. The radiation traveling directly from the bending magnets to the diagnostics system, as well as any other similar direct radiation, was ruled out by blocking the path. Still, it can couple to the beam pipe waveguide modes, land on the OTR screen, and be reflected to the optical channel. For the estimation purposes it can be assumed that all the radiated energy couples to the waveguide. With this assumption, two radiation candidates have the same power dependence on the longitudinal bunch distribution of the bunch as the COTR (here we also assume that the last dipole is the only source of the radiation, and the bunch length change is small both in the dipole and between the dipole and the OTR source). All is left to do is to compare the relative amplitude of these three.

Simple estimates, based on [34] give us the following ratio of CTR:CSR:

$$\frac{dW_{TR}}{\mathrm{d}\omega} : \frac{dW_{SR}}{\mathrm{d}\omega} = \frac{e^2}{4\pi\varepsilon_0 c}\left(\frac{1}{\pi^2}\int_0^{\pi}\frac{\beta^2\sin^3\theta\ \mathrm{d}\theta}{(1-\beta^2\cos^2\theta)^2} : \frac{\sqrt{3}\gamma\omega}{2\omega_c}\int_{\omega/\omega_c}^{\infty}\mathrm{K}_{5/3}(x)\ \mathrm{d}x\right), \tag{22}$$

where $\omega_c = \frac{3}{2}\omega_0\gamma^3$ is the critical frequency, $\omega_0 = \frac{\beta c}{r}$ is the angular frequency of the particles moving in a bending magnet, r is the bend radius, and K is the modified Bessel function. The ratio is 64:1 at $\lambda = 3$ μm, with CSR becoming negligible if the wavelength is even lower.

Generally, the CER is noticeable only if the wavelength is larger than the critical wavelength of the synchrotron radiation, which is 28 μm in our case. Furthermore, in order to be properly reflected and reach the photodiode, the radiation must be within a narrow region of the OTR screen, as discussed in Sec. IV C. Because a general waveguide mode is not tightly constrained within this area, we need to introduce an additional factor of $\frac{r_{\mathrm{PD}}^2}{2r_p^2} \approx 2\times 10^{-4}$ for any radiation generated not on the OTR screen itself. Next, the assumption of perfect collection of synchrotron radiation from the entire fourth dipole and the constant minimal bunch length along the curvature is removed. Finally, the radiation reflected from the OTR screen is subject to the same transverse bunch size factor p, where the "bunch size" should be substituted with the OTR screen radius, which makes the factor even smaller. These factors together, without the transverse bunch size factor, total to a value less than 10^{-5}, effectively damping the radiation amplitude observed on the photodiode, meaning that the signal increase is not due to CSR or CER.

As a result, we state that the signal elevation is indeed caused by a microbunching structure in the bunch, that creates the coherent term in transition radiation spectrum.

VIII. CONCLUSION

We have constructed and analyzed a low-level noise measurement system, collected the experimental data, and compared it with theoretical expectations and simulations. An uncompressed or moderately compressed bunch ($l > 2$ ps) has no additional noise above shot level $F = 1$, which is supported by both experiment and space-charge particle tracking. The experiment covers the range of wavelengths up to $\lambda = 2.5$ μm, while the rest of the EIC CEC significance range is covered by the simulations.

With 67% confidence, the electron diffusion rate is less than 10% of the cooling rate ($\frac{T_{\mathrm{cool}}}{T_{\mathrm{diff}_e}} < 0.1$) according to the experimental uncertainties, and less than 20% of the cooling rate ($\frac{T_{\mathrm{cool}}}{T_{\mathrm{diff}_e}} < 0.2$) according to the simulation uncertainties. Noticeable microbunching starts to appear at $\lambda = 60$ μm. For comparison, the same ratio for the hadron bunch diffusion is $\frac{T_{\mathrm{cool}}}{T_{\mathrm{diff}_h}} = 0.04$.

A compressed bunch ($l \approx 1$ ps), on the contrary, shows large microbunching amplitudes, especially on wavelengths $\lambda > 2.5$ μm, as can be seen from the simulations. The modulations were confirmed experimentally, though only in the spectral segment with smaller increases, as the detector sensitivity extends only up to 3 μm. Extending this comparison to a broader spectral range in future studies could improve the accuracy of the noise level measurement.

An estimation of the transverse bunch size effect on coherence loss in an optical channel was proposed to better align with experimental observations. While this approach proved to be in agreement with experiment when averaged over all filters, comparison with individual filters showed some disagreement.

Future studies could expand the experimental spectral range at higher energies to better align with the requirements of CEC schemes and FELs. These experiments should have precise diagnostics of all the measurement elements and bunch parameters.

ACKNOWLEDGMENTS

This project is supported by a grant (DE-SC0022196) from the DOE ARDAP office. This work was also supported by the U.S. National Science Foundation under Award No. PHY-1549132, the Center for Bright Beams, and by the University of Chicago. This manuscript has been authored by Fermi Research Alliance, LLC under Contract No. DE-AC02-07CH11359 and by Brookhaven Science Associates, LLC under Contract No. DE-SC0012704 with the U.S. Department of Energy, Office of Science. This research used the open-source particle-in-cell code ImpactX [45]. We acknowledge all ImpactX contributors. We are grateful to the UChicago Soft Matter Characterization Facility staff and to Philip Griffin in particular for allowing us to use their spectrophotometer for our work.

DATA AVAILABILITY

The data that support the findings of this article are openly available [33].

APPENDIX A: ELECTRON BUNCH NOISE EFFECTS IN THE EIC CEC SYSTEM

The cooling times with noise effects have been well described in [3] for the noise passing through the amplification sections (and acting in the kicker) and also in [24] for the modulator. Different effects, including the interference between the noise passed through the modulator and the shot noise at the beginning of the amplifiers, are summarized in [4].

We first use Eqs. (39) and (40) from [3] with the EIC CEC parameters from [23] to verify that the parameters used are the same, obtaining 165 min of the cooling time. Next, we calculate the r_2 factor from Eqs. (48), (67), and (68) of the same article to get

$$r_2 = \left.\frac{T_{\rm cool}}{T_{\rm diff_e}}\right|_{\rm shot\text{-}noise} = 0.021. \tag{A1}$$

Now we compare the diffusion rates with and without modulator effects using the impedances provided in Eq. (14) of [4]. In this derivation we follow the notations from [4], including usage of the wave vector $k = (\omega/c)$ and coordinate $z = ct$. It is more convenient not to go to the space domain and utilize the impedances: we transform Eq. (16) from the same article to obtain the change of the hadron bunch energy in one turn:

$$\Delta\eta_{h,i}(z) = \frac{r_h}{\gamma}\int Z_i(k)\delta\rho_i(k)e^{ikz}dk, \tag{A2}$$

where index i corresponds to the terms from Eq. (16) of [4].

By averaging the absolute value squared of (A2) by z and particles i, we arrive to the same answers as in [4], but for an arbitrary noise. For example, for the noise in the electron bunch presented at the entrance to the amplifier, we have:

$$\langle\Delta\eta_h^2\rangle_{e,2} = \left(\frac{r_h}{\gamma}\right)^2 n_e \int |Z_{e,2}(k)|^2|\delta\rho_e(k)|^2 dk. \tag{A3}$$

Note that for the shot-noise bunch the result is the same as in [4] because of the Parseval's theorem. The diffusion rate is defined as

$$\frac{1}{T_{\rm diff}} = \frac{1}{\eta_h^2}\frac{{\rm d}\eta_h^2}{{\rm d}t} = \frac{1}{\eta_h^2}\frac{\langle\Delta\eta_h^2\rangle}{T}, \tag{A4}$$

where T is the turn period. Finally, we use (A3) to derive the ratio of two diffusion rates: caused by the noise at the modulator (1) and by the electron shot noise at the entrance to the amplifier (2):

$$\frac{T_{{\rm diff}_{e,2}}}{T_{{\rm diff}_{e,1}}} = \frac{\int_{-\infty}^{\infty}|Z_{e,1}(k)|^2\,{\rm d}k}{\int_{-\infty}^{\infty}|Z_{e,2}(k)|^2\,{\rm d}k} \approx 0.7\times 10^{-3}. \tag{A5}$$

Therefore, we can safely neglect the effect in the modulator and the interference term, and obtain Eq. (5), with k instead of ω. Of course, transformation to frequencies requires only switching k to ω.

$$\frac{T_{\rm cool}}{T_{\rm diff_e}} = r_2\frac{\int_{-\infty}^{\infty}|Z_{e,2}(k)|^2|\delta\rho_e(k)|^2\,{\rm d}k}{\int_{-\infty}^{\infty}|Z_{e,2}(k)|^2\frac{1}{N}\,{\rm d}k}. \tag{A6}$$

Following the explanation in the introduction, $|\delta\rho_e(\omega)|^2$ can be substituted with $|\rho_e(\omega)|^2$. We can get the bunch spectrum $|\rho_e(\omega)|^2$ from Eq. (13) and express the electron diffusion-to-cooling ratio in terms of the measurements:

$$\frac{T_{\rm cool}}{T_{\rm diff_e}} = r_2\frac{\int_{-\infty}^{\infty}|Z_{e,2}(\omega)|^2\frac{{\rm d}W}{{\rm d}\omega}\,{\rm d}\omega}{\int_{-\infty}^{\infty}|Z_{e,2}(\omega)|^2 N\frac{dW_1}{{\rm d}\omega}\,{\rm d}\omega}, \tag{A7}$$

where $\frac{dW_1}{d\omega}$ is the OTR spectrum from one particle, which does not depend on ω, and $\frac{dW}{d\omega}$ is the OTR spectrum measured experimentally.

Parameters used in the text are presented in Table II.

In the derivation and in the table, we used that the wavelength of the oscillations is much lower than the hadron bunch size in the modulator $k \gg \frac{\gamma}{\sigma_p}$, so that the dimensionless length l can be taken to be constant.

APPENDIX B: SIGNAL PROPAGATION THROUGH THE OPTICAL CHANNEL

Transition radiation generated at the OTR screen is transported through a system with two parabolic mirrors, shown in Fig. 7. The numerical parameters of the channel can be found in Appendix C. We decompose the field at the

TABLE II Main parameters of the electron-ion collider coherent electron cooling (EIC CEC) system.

Parameter	Value
Modulator length L_m, m	40
Kicker length L_k, m	40
Hadron particle charge Z, e	1
Bunch size in the amplifier Σ (h and e), mm	0.67
Electron bunch energy E, MeV	149.8
Electron chicane strength $R_{56,e}$, mm	7.1
Hadron chicane strength $R_{56,h}$, mm	1.95
Electron bunch charge Q_e, nC	1
Hadron bunch charge Q_h, nC	11
Electron bunch rms length $\sigma_{z,e}$, mm	4
Hadron bunch rms length $\sigma_{z,h}$, mm	60
Amplifier to modulator bunch size ratio $r = \frac{\Sigma}{\Sigma_p}$	0.2
Dimensionless length $l = \frac{\pi r}{2}$	1
Dimensionless chicane strength $q = \frac{R_{56}\sigma_\eta \gamma}{\Sigma}$	0.6

OTR screen into plane waves (by applying a Fourier transform) and propagate the plane waves through the system. First, we calculate the field generated by a point at the OTR screen, and then integrate over the whole screen. For a single source point we find that: (i) The bunch is imaged on the photodiode screen such that any ray from a point $\{x_0, y_0\}$ on the OTR screen reaches corresponding coordinates $\{x_1, y_1\} \approx \{-x_0, -y_0\}$ at the photodiode plane. In the discussion below, we omit the minus sign for clarity (but keep it in the calculations). An illustration of the focusing is presented in Fig. 17 left. (ii) The path length from the OTR screen to the photodiode plane ($l_{\{x_0,y_0\}\to\{x_1,y_1\}}$) *plus* the path length of the particle in the bunch from the transverse cross section to the OTR screen ($l_{\{x_b,y_b\}\to\{x_0,y_0\}}$) does not depend on the emission angle θ: $l(\theta) = l_{\{x_b,y_b\}\to\{x_0,y_0\}} + l_{\{x_0,y_0\}\to\{x_1,y_1\}} = l$. The dependence of the path length $l(\theta)$ on the emission location x_0 for different emission angles θ is not written as a formula here because it is lengthy, but is presented in Fig. 17 right. It can be seen that the dependence on θ is weak if $\theta \ll 1$, with phase differences much smaller than the wavelength of interest.

Therefore, the field at the photodiode plane is given by an inverse Fourier transform:

$$\boldsymbol{E}(x,y) = \int \boldsymbol{A}\, J_{\boldsymbol{k}}\, e^{ik_x x + ik_y y} d\theta d\phi = \int \frac{k^2 \sin^2\theta \cos\theta \sin\theta}{(1-\beta^2\cos^2\theta)^2} e^{ik((x-x_0)\sin\theta\cos\phi + (y-y_0)\sin\theta\sin\phi)} d\theta d\phi, \tag{B1}$$

where $J_{\boldsymbol{k}}$ is the Jacobian of the transformation $\{k_x, k_y\} \to \{\theta, \phi\}$, and $\boldsymbol{A} = \boldsymbol{A}(\theta, \phi)$ is the complex amplitude (direct Fourier transform of the electric field at the OTR screen), corresponding to the distribution of the OTR radiation by angle. For estimation purposes, we ignore the dependence of the direction of $\boldsymbol{A}$ on θ and ϕ, as its contribution is only of an order of $1/\gamma^2$.

The spot size is given by

$$\sigma^2_{\text{single}} = \frac{\int x^2 |E(x,0)|^2\, dx}{\int |E(x,0)|^2\, dx}. \tag{B2}$$

It is calculated numerically to give approximately

$$\sigma_{\text{single}} \approx \lambda\gamma. \tag{B3}$$

Before we integrate by the bunch distribution, it is important to understand the geometrical restrictions imposed by the channel. When propagating a ray through the system (using geometric optics), we find the positions of the ray at each element depending on the emission location and angles. By comparing the apertures of the mirrors, vacuum window, filter, and photodiode with these positions, we find the constraints.

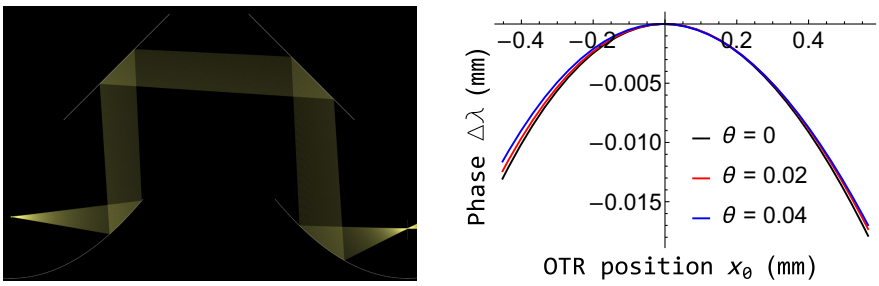


FIG. 17. Left: an illustration of the focusing in a system with two parabolic mirrors. All the rays emitted from a point $\{x_0, y_0\}$ at the OTR screen are focused onto the position $\{-x_0, -y_0\}$ at the photodiode plane. Right: phase shift dependence on the emission location x_0 and the emission angle θ. The phase shift is smaller than the wavelength of interest if the emission angle is varied. The shift within the spot size ($\sigma_{\text{single}} \approx 0.1$ mm, see below) is also smaller than the wavelength.

Comparison of the PD (r_{PD}) and bunch ($\sigma_\perp$) sizes gives very restrictive boundaries for the bunch particle positions: $|x_0|_{\max} = r_{\mathrm{PD}}/\sqrt{2} = 0.35$ mm. The mirrors (and filter) aperture restrictions depend almost solely on the emission angles (only on θ):

$$\theta < r_{\mathrm{PM}} \qquad \theta\, d_f < r_f, \tag{B4}$$

where r_f is the filter radius. The filter aperture appears more restrictive and gives

$$|\theta|_{\max} \approx 0.075. \tag{B5}$$

As can be seen from Fig. 17, it turns out that the total path length l depends weakly on x_0 and y_0 for any small angle. Setting the phase advances to exact zero for estimation purposes, we can easily find the total preservation of coherence, either by integrating by x_0, y_0, or by making estimations as in the main part of the text.

Finally, misalignment of the photodiode and the first parabolic mirror position relative to the OTR source leads to additional dispersion: around 20 μm phase difference per 1 mm misalignment. The parabolic mirror positioning was accurately tuned with precision higher than 0.1 mm, meaning that the misalignment effect can be dropped, leaving only the factor p used in the main part of the article.

An approximate analytical propagation of a ray through the optical channel, with $y_0 = 0$ and $\phi = 0$, is presented below for illustrative purposes. The results described above were obtained with exact expressions, of course.

We work in the accelerator coordinates: z axis is in the direction of the on-symmetry axis (i.e., for the radiation transmitted from the first parabolic mirror focus point into $\phi = 0$, $\theta = 0$ direction), x axis is horizontal, and y axis is vertical. We assume that all elements are centered on the symmetry axis and perfectly aligned, with the OTR source and photodiode located at the focal points of the first and second parabolic mirrors, respectively. The parabolic mirror equation is $y = \frac{1}{4F}x^2$, where F is the focal distance of the mirror.

By applying geometrical optics, we get the ray positions at each mirror (x_1, x_2), at the filter (x_3), and at the photodiode (x_4). For analytical expressions, we write the formulas in the first order in initial position x_0 and emission angle θ:

$$x_1 \approx 2F\tan\theta + x_0(1-\sin\theta), \tag{B6}$$

$$\theta_1 \approx \theta - \frac{x_1}{2F} \approx -\frac{x_0}{2F}, \tag{B7}$$

$$x_2 \approx x_0 + 2F\theta - \frac{x_0 L}{2F}, \tag{B8}$$

$$\theta_2 \approx \theta_1 + \frac{x_2}{2F} \approx -\frac{x_0}{2F} + \theta + \frac{x_0}{2F} - \frac{x_0 L}{4F^2} = \theta - \frac{x_0 L}{4F^2}, \tag{B9}$$

$$x_3 \approx x_0 + d_f\left(\theta - \frac{x_0 L}{4F^2}\right), \tag{B10}$$

$$x_4 \approx x_2 - (2F + x_2)\tan\theta_2 \approx x_0. \tag{B11}$$

APPENDIX C: MAIN PARAMETERS USED IN THE ARTICLE

FAST specifications, important for the X121 cross simulations, are listed in Table III. More detailed information can be found at [46].

Initial bunch (at $z = 0$ m) parameters are listed in Table IV.

Optical channel and detector specifications are listed in Table V.

TABLE III Low energy line FAST specifications.

Parameter	Value
rf cavities (CC1, CC2) length, m	1.435
rf cavities (CC1, CC2) gradient, MeV/m	10–11
Chicane bend radius, cm	0.8425

TABLE IV FAST photocathode ($z = 0$) electron bunch parameters.

Parameter	Value
Macropulse repetition rate, Hz	1–5
Micropulse spacing, ns	333
Micropulse length, ps	3–20
Bunch transverse size, mm	0.1–1.5

TABLE V Optical channel and detector specifications.

Parameter	Value
Screen to first mirror distance $2F$, cm	17.88
First to second mirror distance L, cm	415
Parabolic mirrors aperture r_{PM}, cm	38.1
Photodiode aperture r_{PD}, cm	0.05
Average filter aperture r_f, cm	0.28

[1] W. Schottky, Über spontane stromschwankungen in verschiedenen elektrizitätsleitern, Ann. Phys. (Berlin) **362**, 541 (1918).

[2] W. Schottky, On spontaneous current fluctuations in various electrical conductors, J. Micro/Nanolithogr. MEMS MOEMS **17**, 041001 (2018).

[3] G. Stupakov and P. Baxevanis, Microbunched electron cooling with amplification cascades, Phys. Rev. Accel. Beams **22**, 034401 (2019).

[4] W. F. Bergan, Electron diffusion in microbunched electron cooling, Phys. Rev. Accel. Beams **27**, 084402 (2024).

[5] Z. Huang and K.-J. Kim, Review of x-ray free-electron laser theory, Phys. Rev. ST Accel. Beams **10**, 034801 (2007).

[6] E. L. Saldin, E. A. Schneidmiller, and M. V. Yurkov, Study of a noise degradation of amplification process in a multistage HGHG FEL, Opt. Commun. **202**, 169 (2002).

[7] D. Ratner, Much ado about microbunching: Coherent bunching in high brightness electron beams Ph.D. thesis, Stanford University, Stanford, CA, 2011, https://www.osti.gov/biblio/1043865.

[8] Z. Huang and T. Shaftan, Impact of beam energy modulation on rf zero-phasing microbunch measurements, Technical Report No. SLAC-TN-03-042, SLAC, 2003, https://www.osti.gov/biblio/815284.

[9] Z. Huang and K.-J. Kim, Formulas for coherent synchrotron radiation microbunching in a bunch compressor chicane, Phys. Rev. ST Accel. Beams **5**, 074401 (2002).

[10] S. Heifets, G. Stupakov, and S. Krinsky, Coherent synchrotron radiation instability in a bunch compressor, Phys. Rev. ST Accel. Beams **5**, 064401 (2002).

[11] A. W. Chao, M. Tigner, H. Weise, and F. Zimmermann, *Handbook of Accelerator Physics and Engineering*, 3rd ed. (World Scientific, Singapore, 2023), pp. 192–196, 10.1142/13229.

[12] Y. S. Derbenev, Theory of electron cooling, arXiv:1703.09735.

[13] S. van der Meer, Stochastic damping of betatron oscillations in the ISR, Technical Report No. CERN-ISR-PO-72-31, CERN, 1972, https://cds.cern.ch/record/312939/files/197200067.pdf.

[14] S. van der Meer, Stochastic damping of betatron oscillations, in *The Development of Colliders* (World Scientific, Singapore, 1995), pp. 261–275.

[15] V. Lebedev, High-energy cooling, J. Instrum. **19**, P06015 (2024).

[16] S. Nagaitsev, D. Broemmelsiek, A. Burov, K. Carlson, C. Gattuso, M. Hu, T. Kroc, L. Prost, S. Pruss, M. Sutherland, C. W. Schmidt, A. Shemyakin, V. Tupikov, A. Warner, G. Kazakevich, and S. Seletskiy, Experimental demonstration of relativistic electron cooling, Phys. Rev. Lett. **96**, 044801 (2006).

[17] V. Lebedev, J. Jarvis, H. Piekarz, A. Romanov, J. Ruan, and M. Andorf, The design of optical stochastic cooling for IOTA, J. Instrum. **16**, T05002 (2021).

[18] M. S. Zolotorev and A. A. Zholents, Transit-time method of optical stochastic cooling, Phys. Rev. E **50**, 3087 (1994).

[19] Y. S. Derbenev, On possibilities of fast cooling of heavy particle beams, AIP Conf. Proc. **253**, 103 (1992).

[20] V. N. Litvinenko and Y. S. Derbenev, Coherent electron cooling, Phys. Rev. Lett. **102**, 114801 (2009).

[21] D. Ratner, Microbunched electron cooling for high-energy hadron beams, Phys. Rev. Lett. **111**, 084802 (2013).

[22] S. Nagaitsev, W. F. Bergan, V. Lebedev, G. Stupakov, and E. Wang, Cooling and diffusion rates in coherent electron cooling concepts, in *Proceedings of the 12th International Particle Accelarator Conference (IPAC'21)* (JACoW, Geneva, Switzerland, 2021), pp. 3281–3284, 10.18429/JACoW-IPAC2021-WEPAB273.

[23] F. Willeke and J. Beebe-Wang, Electron-ion collider conceptual design report, 2021, 10.2172/1765663.

[24] G. Stupakov, Cooling rate for microbunched electron cooling without amplification, Phys. Rev. Accel. Beams **21**, 114402 (2018).

[25] G. Stupakov, Noise amplification in HGHG seeding, Technical Report No. SLAC-PUB-14225, SLAC, 2010, https://www.slac.stanford.edu/pubs/slacpubs/14000/slac-pub-14225.pdf.

[26] R. Ianconescu, A. Gover, E. Hemsing, A. Marinelli, and A. Nause, Sub-radiance and enhanced radiance of undulator radiation from a correlated electron beam, in *Proceedings of the 37th International Free Electron Laser Conference (FEL'15), Daejeon, South Korea* (JACoW, Geneva, Switzerland, 2015), MOP078, 10.18429/JACoW-FEL2015-MOP078.

[27] V. Litvinenko, Suppression of shot noise and spontaneous radiation in electron beams, in *Proceedings of the Free Electron Laser Conference (FEL'09), Liverpool, United Kingdom* (JACoW, Geneva, Switzerland, 2009), https://www.osti.gov/biblio/970529.

[28] A. Nause, E. Dyunin, and A. Gover, Short-wavelength limits of current shot-noise suppression, Phys. Plasmas **21**, 083114 (2014).

[29] A. Gover, A. Nause, E. Dyunin, and M. Fedurin, Beating the shot-noise limit, Nat. Phys. **8**, 877 (2012).

[30] Z. Huang and G. Stupakov, Control and application of beam microbunching in high-brightness linac-driven free-electron lasers, Nucl. Instrum. Methods Phys. Res., Sect. A **907**, 182 (2018).

[31] H. Loos, R. Akre, A. Brachmann, F.-J. Decker, Y. Ding, D. Dowell, P. Emma, J. Frisch, S. Gilevich, G. Hays, P. Hering, Z. Huang, R. Iverson, C. Limborg, A. Miahnahri, S. Molloy, H.-D. Nuhn, J. Turner, J. Welch, and S. Menlo, Observation of coherent optical transition radiation in the LCLC linac, in *Proceedings of the 30th International Free Electron Laser Conference (FEL'08)* (2008), https://inspirehep.net/literature/798382.

[32] S. Nagaitsev *et al.*, Noise in intense electron bunches, in *Proceedings of the 5th North American Particle Accelerator Conference (NAPAC'22)* (JACoW, Geneva, Switzerland, 2022), pp. 128–131, 10.18429/JACoW-NAPAC2022-MOPA34.

[33] S. Kladov, Near-Infrared noise in intense electron bunches: Data (2025), 10.5281/zenodo.17985878.

[34] H. Wiedemann, *Particle Accelerator Physics*, 4th ed. (Springer, Cham, 2015), 10.1007/978-3-319-18317-6.

[35] L. D. Landau and E. M. Lifshitz, The passage of fast particles through matter, in *Electrodynamics of Continuous Media, Course of Theoretical Physics*, 2nd ed. (Pergamon, Amsterdam, 1984), Vol. 8, pp. 394–412, 10.1016/B978-0-08-030275-1.50020-5.

[36] G. L. Orlandi, Spatial coherence in the transition radiation spectrum, Opt. Commun. **267**, 322 (2006).

[37] E. Chiadroni, M. Castellano, A. Cianchi, K. Honkavaara, and G. Kube, Effects of transverse electron beam size on

transition radiation angular distribution, Nucl. Instrum. Methods Phys. Res., Sect. A **673**, 56 (2012).

[38] A. Nause, E. Dyunin, R. Ianconescu, and A. Gover, Exact theory of optical transition radiation in the far and near zones, J. Opt. Soc. Am. B **31**, 2438 (2014).

[39] A. Nause, R. Ianconescu, and A. Gover, Correlated electron-beam microbunching and shot-noise characterization with near- and far-field optical transition radiation, J. Opt. Soc. Am. B **35**, 2869 (2018).

[40] A. H. Lumpkin, R. J. Dejus, and N. S. Sereno, Coherent optical transition radiation and self-amplified spontaneous emission generated by chicane-compressed electron beams, Phys. Rev. ST Accel. Beams **12**, 040704 (2009).

[41] A. Tremaine, J. B. Rosenzweig, S. Anderson, P. Frigola, M. Hogan, A. Murokh, C. Pellegrini, D. C. Nguyen, and R. L. Sheffield, Observation of self-amplified-spontaneous-emission-induced electron-beam microbunching using coherent transition radiation, Phys. Rev. Lett. **81**, 5816 (1998).

[42] S. Wesch, C. Behrens, B. Schmidt, and P. Schmüser, Observation of coherent optical transition radiation and evidence for microbunching in magnetic chicanes, in *Proceedings of the 31st International Free Electron Laser Conference (FEL'09), Liverpool, United Kingdom* (JACoW, Geneva, Switzerland, 2009), pp. 619–622, https://www.researchgate.net/publication/40651667_Observation_of_Coherent_Optical_Transition_Radiation_and_Evidence_for_Microbunching_in_Magnetic_Chicanes_2009-08-23_-_2009-08-28.

[43] K. Floettmann, ASTRA: A space-charge tracking algorithm, Technical Report No. DESY-97-047, DESY, 1997, https://www.desy.de/~mpyflo/.

[44] A. Huebl *et al.*, Next-generation computational tools for the modeling and design of particle accelerators at exascale, arXiv:2208.02382.

[45] https://github.com/ECP-WarpX/impactx.

[46] NIUaard, Input decks for elegant, ASTRA to simulate the fast electron-linac beamline, GitHub repository, https://github.com/NIUaard/FAST (2021).